Laser-Induced Magnetization Precession in Individual Magnetoelastic Domains of a Multiferroic $Co_{40}Fe_{40}B_{20}/BaTiO_3$ Composite

L.A. Shelukhin,[1,*] N. A. Pertsev,[1] A.V. Scherbakov,[1,2] D.L. Kazenwadel,[3] D.A. Kirilenko,[1] S.J. Hämäläinen,[4] S. van Dijken,[4] and A.M. Kalashnikova[1]

[1] *Ioffe Institute, St. Petersburg 194021, Russia*

[2] *Experimental Physics II, Technical University Dortmund, Dortmund D-44227, Germany*

[3] *University of Konstanz, Konstanz D-78457, Germany*

[4] *NanoSpin, Department of Applied Physics, Aalto University School of Science, P.O. Box 15100, Aalto FI-00076, Finland*

(Received 9 April 2020; revised 15 July 2020; accepted 14 August 2020; published 23 September 2020)

Using a magneto-optical pump-probe technique with micrometer spatial resolution, we show that magnetization precession can be launched in individual magnetic domains imprinted in a $Co_{40}Fe_{40}B_{20}$ layer by elastic coupling to ferroelectric domains in a $BaTiO_3$ substrate. The dependence of the precession parameters on the strength and orientation of the external magnetic field reveals that laser-induced ultrafast partial quenching of the magnetoelastic coupling parameter of $Co_{40}Fe_{40}B_{20}$ by approximately 27% along with 10% ultrafast demagnetization triggers the magnetization precession. The relation between the laser-induced reduction of the magnetoelastic coupling and the demagnetization is approximated by an $n(n+1)/2$ law with $n \approx 2$. This correspondence confirms the thermal origin of the laser-induced anisotropy change. Based on analysis and modeling of the excited precession, we find signatures of laser-induced precessional switching, which occurs when the magnetic field is applied along the hard magnetization axis and its value is close to the effective magnetoelastic anisotropy field. The precession-excitation process in an individual magnetoelastic domain is found to be unaffected by neighboring domains. This makes laser-induced changes of magnetoelastic anisotropy a promising tool for driving magnetization dynamics and switching in composite multiferroics with spatial selectivity.

DOI: 10.1103/PhysRevApplied.14.034061

I. INTRODUCTION

Magnetoelectric multiferroics offer the possibility of controlling magnetization with an electric field [1–3], that is in high demand for technologies beyond CMOS [4], including sensors, energy harvesters, memories, and logic devices [5]. However, the number of single-phase multiferroics is limited [6], with many of these materials exhibiting multiferroic properties below room temperature or providing insufficient coupling between the order parameters. On the other hand, composite structures consisting of ferromagnetic (FM) and ferroelectric (FE) materials coupled via strain represent a promising alternative way of achieving indirect magnetoelectric coupling at room temperature, of sufficient strength for future applications [5,7–10].

In strain-coupled composite multiferroics, the magnetic anisotropy of the FM component is altered by a combination of interfacial strain transfer from the FE component and inverse magnetostriction. For properly selected FM and FE materials, heterostructure geometries, and optimized interfaces, strong magnetization responses to external electric fields can be obtained. In particular, full imprinting of ferroelastic domain patterns from FE substrates into FM overlayers with in-plane and perpendicular magnetizations and their subsequent manipulation by electric fields have been demonstrated experimentally [11–17]. FM-FE composites enable electric-field-induced magnetization switching, leading to changes in magnetoresistance [18–22], electrical tuning of ferromagnetic resonances and spin-wave spectra [23–26], active filtering and routing of propagating spin waves [27,28], and electrical switching between superconducting and normal states [29].

Control of the order parameters of composite multiferroic structures by femtosecond laser pulses would widen the range of application of such materials and elevate their switching speed. There are several pathways by which an ultrafast optical stimulus may alter the state of a composite multiferroic. One of them relies on ultrafast direct optical control of the magnetization [30] and, via FM-FE coupling, of the ferroelectric polarization [31,32]. Alternatively, ultrafast optically driven changes of the FE state could lead to high-amplitude dynamic strain modulations

*shelukhin@mail.ioffe.ru

[33] and, thus, alter the magnetization state of a magnetostrictive layer. However, ultrafast optical control of FE polarization remains challenging [34]. Optically induced strain was considered as a tool to modify the magnetic anisotropy in FM-photostrictive composites in Ref. [35], but the results reported thus far do not extend to ultrafast time scales.

In this paper, we examine an alternative approach to ultrafast optical control of a composite multiferroic and study the feasibility of using ultrafast laser-induced changes of the strain-mediated magnetoelectric coupling in a $Co_{40}Fe_{40}B_{20}/BaTiO_3$ heterostructure. Using a femtosecond magneto-optical pump-probe technique with micrometer spatial resolution, we excite magnetization precession in individual magnetic domains imprinted in an amorphous $Co_{40}Fe_{40}B_{20}$ layer by mechanical coupling to ferroelastic domains in $BaTiO_3$. We reveal that the precession is triggered by an abrupt decrease in the magnetoelastic coupling parameter and magnetization of the $Co_{40}Fe_{40}B_{20}$ by about 27% and 10%, respectively, for an incident laser pulse fluence of 10 mJ/cm^2. This ratio satisfies an $n(n+1)/2$ law with $n \approx 2$, which describes the temperature-induced variations of the single-ion uniaxial magnetic anisotropy, confirming the thermal origin of the observed changes. When the magnetic field is applied along the hard anisotropy axis and is comparable to the effective magnetoelastic anisotropy field, we find signatures of precessional switching of the magnetization. The switching is manifested in the suppression of the detected pump-probe signal.

This paper is organized as follows. In Sec. II, we describe the $Co_{40}Fe_{40}B_{20}/BaTiO_3$ heterostructure studied and the experimental procedures. In Sec. III, we present experimental results on laser-induced magnetization precession in individual domains in the $Co_{40}Fe_{40}B_{20}/BaTiO_3$ structure. In Sec. IV, we present an analysis of the laser-induced precession based on a thermodynamic approach and the Landau-Lifshitz-Gilbert (LLG) equation. This is followed by a Conclusions section, where we outline possible applications of laser-induced control of magnetoelastic anisotropy in spintronics.

II. EXPERIMENTAL DETAILS

A. $Co_{40}Fe_{40}B_{20}/BaTiO_3$ heterostructure

The heterostructure under study consists of a 50-nm-thick layer of a FM $Co_{40}Fe_{40}B_{20}$ amorphous alloy on a 500-μm-thick single-crystalline $BaTiO_3$ (001) substrate. The $Co_{40}Fe_{40}B_{20}$ layer is grown on the $BaTiO_3$ by magnetron sputtering at $T_g = 573$ K and capped with a 6-nm-thick Au layer. The amorphous nature of the $Co_{40}Fe_{40}B_{20}$ film is verified by transmission electron microscopy. Figures 1(c) and 1(d) show TEM images of the $Co_{40}Fe_{40}B_{20}/BaTiO_3$ heterostructure. Cross-sectional TEM specimen are prepared by mechanical polishing and subsequent Ar^+ ion milling at 3 keV. A Jeol JEM-2100F microscope operated at 200 kV is used to acquire images in the conventional bright-field and high-resolution modes. The TEM images indicate that the $Co_{40}Fe_{40}B_{20}$ film is amorphous, with a short-range order corresponding to a length scale of approximately 1 nm.

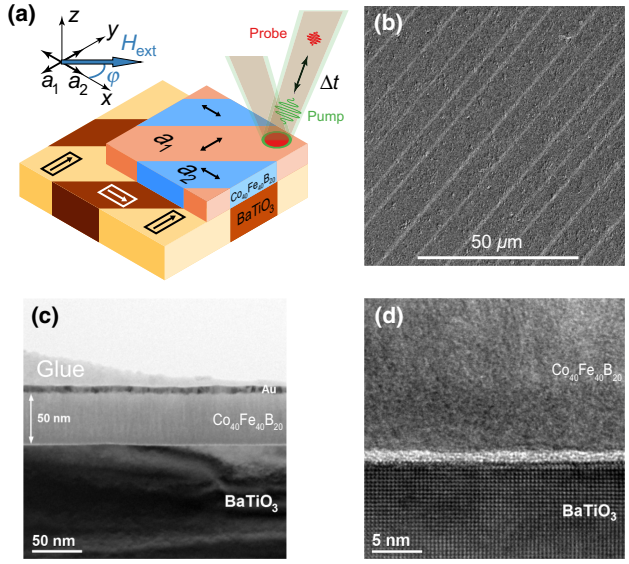

FIG. 1. (a) Schematic illustration of the $Co_{40}Fe_{40}B_{20}/BaTiO_3$ structure and the pump-probe experiment. The arrows in rectangles and the double-headed arrows indicate the spontaneous polarization in the ferroelastic domains of the $BaTiO_3$ and the strain-induced magnetic anisotropy axes of the a_1 and a_2 domains in the $Co_{40}Fe_{40}B_{20}$ layer, respectively. (b) Magneto-optical image of a sample obtained using longitudinal Kerr microscopy. (c) Bright-field and (d) high-resolution TEM images of the $Co_{40}Fe_{40}B_{20}/BaTiO_3$ heterostructure.

At room temperature, the $BaTiO_3$ substrate is split into 90° ferroelectric-ferroelastic stripe domains with an in-plane spontaneous polarization aligned along the long side of the tetragonal unit cell [12]. Owing to strain transfer from the $BaTiO_3$ to the $Co_{40}Fe_{40}B_{20}$ and inverse magnetostriction, a uniaxial magnetoelastic anisotropy is locally induced in the $Co_{40}Fe_{40}B_{20}$ film. Since the magnetostriction parameter λ of $Co_{40}Fe_{40}B_{20}$ is positive, the easy axes of the magnetic anisotropy are oriented parallel to the polarizations of the underlying FE domains [12,14] [Fig. 1(a)]. The strain-induced magnetoelastic anisotropy dominates over other contributions to the anisotropy, and, consequently, the stripe domains in the $Co_{40}Fe_{40}B_{20}$ and $BaTiO_3$ are fully correlated.

The magnetoelastic domain pattern in $Co_{40}Fe_{40}B_{20}$ is imaged by magneto-optical Kerr microscopy (see Ref. [12] for details). As can be seen from the image in Fig. 1(b), the two types of domain have different widths. The width of the wider domains varies around 12 μm, while the width

of the narrow domains is about 3 μm. The two domain types are labeled a_1 and a_2, respectively [see Fig. 1(a)].

B. Magneto-optical pump-probe setup

The laser-induced magnetization dynamics in distinct magnetic domains of the $Co_{40}Fe_{40}B_{20}/BaTiO_3$ composite is studied using a femtosecond two-color magneto-optical pump-probe setup. In the experiments, the duration of the pump and probe pulses is 170 fs, the central wavelengths of the pump and probe pulses are 515 and 1030 nm, respectively, the pump pulse fluence is 10 mJ/cm^2, and the probe pulse fluence is approximately 10 times lower. Both the pump and the probe pulses are focused into a spot on the $Co_{40}Fe_{40}B_{20}$ layer with a diameter below 5 μm using a 15$\times$ reflective microscope objective. The laboratory frame is chosen such that the x, y, and z axes are directed along the easy axes of the a_2 and a_1 domains and the sample normal, respectively [Fig. 1(a)]. An external dc magnetic field $\mathbf{H}_{\text{ext}}$ of strength 0–120 mT is applied in the sample plane at an angle φ to the x axis. Measurements of the laser-induced magnetization dynamics at $\varphi = 0, \pm 45^\circ$ in the a_1 and a_2 domains are performed by displacing the sample laterally with 0.05-μm precision. The pump-induced changes of magnetization are traced by recording the magneto-optical Kerr rotation $\Delta\theta$ of the probe polarization plane as a function of the time delay Δt between the pump and probe pulses. The incidence angle of the probe pulses is $\zeta = 17^\circ$, and the measured Kerr rotation $\Delta\theta(\Delta t)$ is mostly proportional to the pump-induced changes of the out-of-plane component M_z of the magnetization. All measurements are performed at room temperature.

Additional static magneto-optical characterization and pump-probe studies of laser-induced demagnetization are performed with larger laser spots. Since the easy magnetization axes lie in the sample plane, the static magneto-optical and the ultrafast demagnetization measurements are conducted in the longitudinal magneto-optical-Kerr-effect (MOKE) geometry with a probe incidence angle $\zeta = 45^\circ$. The pump is incident along the sample normal. Long-focal-distance lenses are used to focus the pump and probe pulses into spots on the sample surface with diameters of 60 and 30 μm, respectively. Since the spot sizes in these experiments exceed the widths of both the a_1 and the a_2 domains, an external magnetic field $H_{\text{ext}} =$ 150 mT is applied along the easy axis of the anisotropy of the a_1 domains to fully saturate the magnetization of the sample into a single-domain state. In this case, the MOKE signal is proportional to the saturation magnetization M_S. The incident probe pulses are p-polarized to maximize the longitudinal MOKE response. Static MOKE measurements without pump pulses reveal a static Kerr rotation $\theta_S^L = 2.5$ mdeg and a Kerr ellipticity $\epsilon_S = 20$ mdeg at saturation. To study ultrafast demagnetization, the laser-induced dynamics of the probe ellipticity $\Delta\epsilon(\Delta t) \sim \Delta M_S(\Delta t)$ is measured after excitation of the sample by pump pulses with a fluence $F = 10$ mJ/cm^2. The degree of ultrafast demagnetization is calculated as $\Delta M_S(\Delta t)/M_S = 0.5[\Delta\epsilon(\Delta t, +H_{\text{ext}}) - \Delta\epsilon(\Delta t, -H_{\text{ext}})]/\epsilon_S$.

The longitudinal Kerr rotation θ_S^L and Kerr ellipticity ϵ_S are also used to estimate the polar Kerr rotation $\theta_S^P \approx$ 15 mdeg corresponding to magnetization saturation along the perpendicular direction (see Appendix A for details). θ_S^P is used to normalize the dynamic Kerr rotation $\theta(\Delta t)$ obtained in the pump-probe experiments and to obtain the magnitude of the laser-induced change of the magnetization along the z axis, $\Delta M_z(\Delta t)/M_S = \Delta\theta(\Delta t)/\theta_S^P$. We note that the estimated value of θ_S^P contains an uncertainty (see Appendix A).

III. RESULTS

Figure 2(a) shows the laser-induced rotation $\Delta\theta(\Delta t)$ of the probe polarization measured for different positions x of the laser spots on the sample surface. We note that a translation along the x axis corresponds to a translation by $x\sqrt{2}/2$ along the direction normal to the domain wall. The external magnetic field $\mathbf{H}_{\text{ext}}$ is parallel (perpendicular) to the easy axis of the a_2 (a_1) domains ($\varphi = 0$). At $H_{\text{ext}} = 30$ mT, one can clearly distinguish two types of dynamic

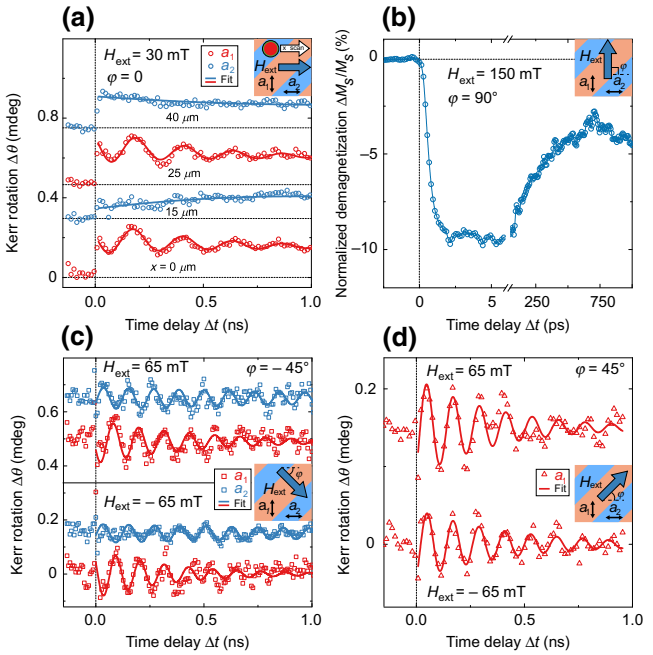

FIG. 2. (a),(c),(d) Laser-induced Kerr rotation $\Delta\theta$ of the probe-pulse polarization as a function of the time delay Δt measured in the a_1 (red symbols) and a_2 (blue symbols) domains. The external magnetic field $\mathbf{H}_{\text{ext}}$ is applied at (a) $\varphi = 0$, (c) $\varphi = -45^\circ$, and (d) $\varphi = 45^\circ$. In (c),(d), the signals measured at positive (upper curves) and negative (lower curves) H_{ext} are shown. The lines are fits to the measurement data (see text). (b) Ultrafast demagnetization measured at $H_{\text{ext}} = 150$ mT.

signal $\Delta\theta(\Delta t)$ depending on x. At $x = 0$ and 25 μm, clear oscillations of $\Delta\theta$ are observed, while at $x = 15$ and 40 μm only a slowly varying change of $\Delta\theta$ is seen. Detailed studies of $\Delta\theta(\Delta t)$ at $x = 0$ for different magnetic field strengths reveal that the oscillatory signal is present only in the range 0–45 mT. The amplitude and frequency of the oscillations as a function of the applied magnetic field are obtained by fitting the signal at $x = 0$ to the function $\Delta\theta(\Delta t) = \Delta\theta_0 \exp(-t/\tau_d)\sin(2\pi ft + \xi_0) + P_2(t)$, where $\Delta\theta_0$, f, ξ_0, and τ_d are the amplitude, frequency, initial phase, and decay time, respectively, of the oscillations. The second-order polynomial function $P_2(t)$ accounts for a slowly varying background of nonmagnetic nature.

The field dependence of the frequency f [Fig. 3(a)] resembles that of magnetization precession in a field applied perpendicular to the easy axis. Therefore, the signal at $x = 0$ can be confidently ascribed to laser-induced precession of the magnetization in the a_1 domains. The periodicity and width of the areas in which laser-induced precession is detected (at $x = 0$ and 25 μm) and not detected (at $x = 15$ and 40 μm) correspond to the length scale of the magnetic domain pattern in the sample. The field dependence of the change in the out-of-plane magnetization component $\Delta M_z^0/M_S = \Delta\theta^0/\theta_S^P$ is shown in Fig. 3(c).

If the external field $\mathbf{H}_{\text{ext}}$ is applied at an angle $\varphi = -45°$, i.e., if it makes angles of $\pm 45°$ with the easy axes of the a_1 and a_2 domains, a laser-induced precession is observed in both stripe domains over a wider field range. Figure 2(c) shows $\Delta\theta(\Delta t)$ measured in the a_1 (red symbols) and the a_2 (blue symbols) domains at $H_{\text{ext}} = \pm 65$ mT. As one can see, upon the transition from an a_1 to an a_2 domain the initial phase ξ_0 of the magnetization precession changes by 180°. A change in sign of the magnetic field, however, does not affect the character of the precession excited. The dependence of the precession frequency on the field strength [Fig. 3(b)] is typical for a geometry in which the field is applied at 45° with respect to the uniaxial magnetic anisotropy axis and, because of symmetry, is the same for both domains. The precession amplitude shows small variations with the strength of the applied field and is somewhat higher in the wider a_1 domains [see the inset of Fig. 3(d)]. When the external field is applied at $\varphi = 45°$, a laser-induced precession is detected in the a_1 domains only [Fig. 2(d)]. The field dependences of the precession frequency and amplitude are similar to those found in the a_1 domains at $\varphi = -45°$ [Figs. 3(b) and 3(d)].

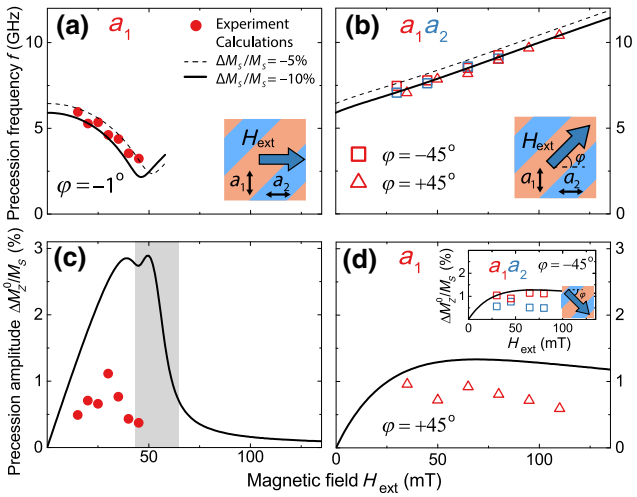

FIG. 3. Experimental magnetic field dependence of the precession frequency f (a),(b) and the normalized amplitude $\Delta M_z^0/M_S$ (c),(d) in the a_1 (red symbols) and a_2 (blue symbols) domains at (a),(c) $\varphi = -1°$ and (b),(d) $\varphi = -45°$ (open squares) and $\varphi = 45°$ (triangles). The solid and dashed lines show the calculated dependences for an a_1 domain, for $\Delta M_S/M_S = -10\%$ and $\Delta M_S/M_S = -5\%$, respectively.

The magnetization precession in the individual domains excited at $\varphi = 0$ and $-45°$ agrees with the general scenario of laser-induced changes of the magnetic anisotropy [36,37]. As discussed in detail in, e.g., Ref. [38,39], a fast change of the effective anisotropy field produces a magnetization precession. The efficiency of excitation is highly sensitive to the alignment of the equilibrium magnetization with respect to the easy anisotropy axis. In our experiments, magnetization precession in a particular domain is not excited when the external field is aligned along the easy anisotropy axis of the domain [Fig. 2(a)]. When the field is aligned perpendicular to the easy anisotropy axis of the domain, the precession is excited only if the field strength is below the anisotropy field. The latter is easily identified in our experiments as the field at which the frequency of the precession is minimum [Fig. 3(a)]. Finally, when the magnetic field is at an intermediate angle to the easy anisotropy axis, e.g., at $\pm 45°$, the magnetization precession is excited over a wider field range [Fig. 3].

Below, we use a macrospin model to analyze the process of excitation and the subsequent decay of the magnetization precession in order to identify the underlying excitation mechanism. In the analysis, we focus mostly on the a_1 domains and neglect effects on the laser-induced dynamics imposed by dipolar coupling to neighboring domains. This is justified by the experimental results, which show that the frequencies of the excited precession in the a_1 and a_2 domains at $\varphi = \pm 45°$ are equal. The difference in the precession amplitudes detected in the a_1 and a_2 domains at $\varphi = -45°$ [Figs. 2(c) and 3(d)] could originate from the fact that the width of the a_2 domains is somewhat smaller than the probe spot size. As a result, the probe measures the magnetization dynamics of an a_2 domain and part of the neighboring a_1 domains, where the precession phase ξ_0 is opposite. This reduces the overall detected transient Kerr rotation. The effect is even more pronounced at $\varphi = +45°$, where no precession signal from an a_2 domain is detected.

In this case, the field is applied along the stripe domains, which initializes head-to-head and tail-to-tail domain walls with a width of about 1.5 μm [27]. As this width is comparable to the width of an a_2 domain, the magnetization in the narrow a_2 domain is nonuniform, which suppresses the measured signal. For the wider a_1 domains or for field orientations that initialize narrow head-to-tail domain walls, a similar reduction of the precession signal does not occur.

IV. DISCUSSION

A. Magnetic anisotropy of the $Co_{40}Fe_{40}B_{20}/BaTiO_3$ heterostructure

In contrast to the metallic films with a pronounced magnetocrystalline anisotropy considered in Ref. [36,37] and subsequent studies, the magnetic anisotropy of amorphous $Co_{40}Fe_{40}B_{20}$ films is fully dominated by a uniaxial magnetoelastic anisotropy. Hence the magnetization-dependent part of the free-energy density F in an individual domain contains only Zeeman, magnetoelastic, and shape-anisotropy terms and can be approximated by the relation [40]

$$F = -\mu_0 \mathbf{M}_S \cdot \mathbf{H}_{\text{ext}} + B_1 \left(u_{xx} m_x^2 + u_{yy} m_y^2\right) + \left[\frac{1}{2}\mu_0 M_S^2 - \frac{c_{12}}{c_{11}} B_1 (u_{xx} + u_{yy})\right] m_z^2, \quad (1)$$

where $m_i = M_i/M_S$, u_{xx} and u_{yy} are the substrate-induced in-plane strains in the $Co_{40}Fe_{40}B_{20}$ film, $B_1 = -1.5\lambda(c_{11} - c_{12})$ is the magnetoelastic coupling parameter, and $c_{11} = 2.8 \times 10^{11}$ N/m^2 and $c_{12} = 1.4 \times 10^{11}$ N/m^2 are the elastic stiffnesses of $Co_{40}Fe_{40}B_{20}$ at a constant magnetization $\mathbf{M}_S$, taken to be those of $Fe_{60}Co_{40}$ [41]. The misfit strains u_{xx} and u_{yy} are expected to be fully relaxed at the growth temperature $T_g = 573$ K, which is well above the Curie temperature $T_C = 393$ K of $BaTiO_3$. On cooling from T_g, nonzero strains appear in the film owing to the difference in the thermal expansion coefficients of paraelectric $BaTiO_3$, $\alpha_0 = 10 \times 10^6$ K^{-1} [42], and $Co_{40}Fe_{40}B_{20}$, $\alpha_b = 12 \times 10^6$ K^{-1} [43]. Taking into account the fact that spontaneous strains appear in $BaTiO_3$ below T_C, we obtain $u_{xx}(T) = a(T)a_0(T_g)^{-1}[1 + \alpha_b(T - T_g)]^{-1} - 1$ and $u_{yy}(T) = c(T)a_0(T_g)^{-1}[1 + \alpha_b(T - T_g)]^{-1} - 1$ for an a_1 domain, and vice versa for an a_2 domain. Here c, a, and a_0 are the lattice constants of the tetragonal FE and cubic paraelectric phase, respectively, of $BaTiO_3$. We obtain $u_{xx} \approx -2.9 \times 10^{-3}$ and $u_{yy} \approx +7.9 \times 10^{-3}$ for an a_1 domain at room temperature by taking $c = 0.4035$ nm, $a = 0.3992$ nm [44], and $a_0(T_g) = 0.4017$ nm [45].

The additional in-plane anisotropy originating from the stripe shape of the domains has been shown to be negligible [12] and is not included in Eq. (1). The orientation of the magnetization in an a_1 domain is defined by the total effective field, which is the sum of the external field $\mathbf{H}_{\text{ext}}$, the effective magnetoelastic anisotropy field $\mathbf{H}_{\text{ME}}$, and the out-of-plane effective field $\mathbf{H}_{\text{out}}$:

$$\begin{aligned}\mathbf{H}_{\text{eff}} &= -\frac{\partial F}{\mu_0\, \partial \mathbf{M}} = \mathbf{H}_{\text{ext}} + \mathbf{H}_{\text{ME}} + \mathbf{H}_{\text{out}} \\ &= \mathbf{H}_{\text{ext}} - \frac{2B_1}{\mu_0 M_S}\left(u_{xx}\mathbf{m}_x + u_{yy}\mathbf{m}_y\right) \\ &\quad + \left[-M_S + \frac{2B_1}{\mu_0 M_S}(u_{xx} + u_{yy})\frac{c_{11}}{c_{12}}\right]\mathbf{m}_z, \quad (2)\end{aligned}$$

where $\mathbf{m}_i = m_i \mathbf{e}_i$, with the $\mathbf{e}_i$ being unit vectors directed along the coordinate axes.

B. Laser-induced change of magnetoelastic anisotropy

The light penetration depth in the $Co_{40}Fe_{40}B_{20}$ layer is below 20 nm at the pump wavelength of 515 nm, and, therefore, we argue that the anisotropy changes are caused by laser-induced processes in the FM film but not by changes in the FE substrate. Excitation of the metallic $Co_{40}Fe_{40}B_{20}$ film by a femtosecond laser pulse results in a rapid increase in the temperatures of the electronic and ionic systems, which equilibrate after several picoseconds. This yields, first of all, ultrafast demagnetization, i.e., a subpicosecond decrease ΔM_S of the saturation magnetization [46] followed by partial restoration upon equilibration between the ionic and electronic temperatures [47]. The ultrafast demagnetization ΔM_S increases the magnetoelastic anisotropy field $H_{\text{ME}} \propto M_S^{-1}$. However, a rapid rise in the film temperature following excitation by a laser pulse should also lead to a decrease ΔB_1 in the temperature-dependent magnetoelastic coupling parameter B_1. In contrast to the ultrafast demagnetization, this reduces the effective magnetoelastic field $H_{\text{ME}} \propto B_1$. Finally, the laser-induced heating ΔT modifies the substrate-induced film strains u_{xx} and u_{yy} via the term $\alpha_b \Delta T$ accounting for the thermal expansion of $Co_{40}Fe_{40}B_{20}$, while the substrate temperature does not change significantly in our case. The resulting variations Δu_{xx} and Δu_{yy} could alter the in-plane field $\mathbf{H}_{\text{ME}} \propto (u_{xx}\mathbf{m}_x + u_{yy}\mathbf{m}_y)$ in addition. As can be seen from Eq. (2), the changes ΔM_S, ΔB_1, and $\Delta u_{xx(yy)}$ affect the out-of-plane anisotropy field $\mathbf{H}_{\text{out}}$ and launch precession if $\mathbf{H}_{\text{out}}$ is nonzero in the initial state [48], which is not the case in our experiments.

In order to verify whether laser-induced changes of the in-plane magnetoelastic anisotropy can indeed account for the observed magnetization precession and to reveal which of the three contributions dominates, we perform numerical calculations. The amplitude of the excited precession is defined by the maximum azimuthal angle $\Delta\psi_{\text{eff}}$ by which the total effective field $\mathbf{H}_{\text{eff}}$ reorients as a result of the laser-induced changes ΔM_S, ΔB_1, and $\Delta u_{xx(yy)}$ [see the insets in Figs. 4(b) and 4(e)]. In the experiments, out-of-plane

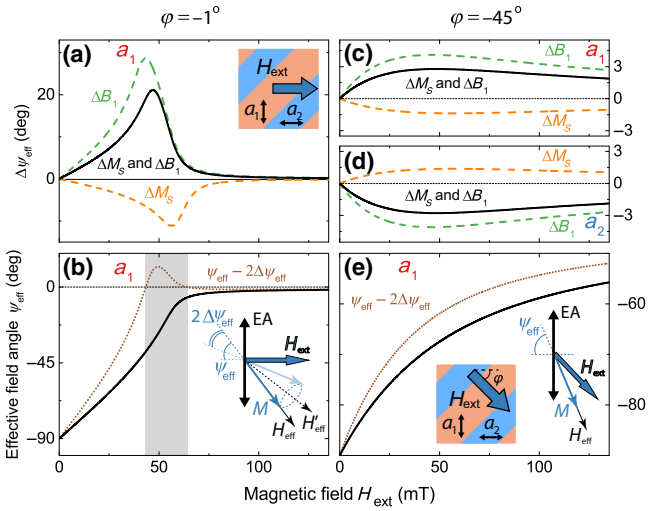

FIG. 4. (a),(b) Calculated field dependence of the orientation change $\Delta\psi_{\text{eff}}$ of the equilibrium effective field $\mathbf{H}_{\text{eff}}$ in the a_1 (a),(c) and a_2 (d) domains due to the laser-induced demagnetization ΔM_S (orange dashed line), the change of the magnetoelastic parameter ΔB_1 (green dashed line), and the total laser-induced effect resulting from ΔM_S, ΔB_1, and $\Delta u_{xx(yy)}$ (solid black line). EA stands for easy axis. (b),(e) Calculated field dependence of the orientation ψ_{eff} of the equilibrium effective field $\mathbf{H}_{\text{eff}}$ (solid black line) and maximum deviation of the magnetization from the x axis in the a_1 domain, $\psi_{\text{eff}} - 2\Delta\psi_{\text{eff}}$ (dotted brown line). The external field $\mathbf{H}_{\text{ext}}$ is applied in (a),(b) at $\varphi = -1^\circ$ and in (c)–(e) at $\varphi = -45^\circ$.

oscillations of the magnetization are detected, and their amplitude can be found from $\Delta M_z^0/M_S = \varsigma\,\Delta\psi_{\text{eff}}$, where ς is the precession ellipticity [49]. The precession frequency is governed by the external magnetic field, the partially quenched magnetization, and the modified magnetoelastic anisotropy within the laser excitation area. On the time scale of the precession, approximately 1 ns, the temperature within the excited spot, the degree of magnetization quenching, and the magnetic anisotropy may vary. However, if the changes in the magnetic parameters of a medium are small, the Smit-Suhl formulas [50,51] can be used to calculate the precession frequency in a first-order approximation.

The degree of demagnetization is obtained experimentally. Figure 2(b) shows the dynamics of the ultrafast demagnetization $\Delta M_S(\Delta t)/M_S$ measured at a pump fluence $F = 10$ mJ cm^{-2}. $\Delta M_S/M_S$ reaches -10% within 2 ps after excitation. This is followed by slow restoration of the magnetization. After 1 ns, the residual demagnetization is -5%.

Since a quasiequilibrium between the electronic, ionic, and spin systems is established several picoseconds after excitation, we assume that for $\Delta t > 2$ ps the laser-induced change of the magnetoelastic parameter B_1 is related to the demagnetization via the thermodynamic relation $B_1(T)/B_1(T=0) = [M_S(T)/M_S(T=0)]^{n(n+1)/2}$ [52]. For the uniaxial magnetoelastic anisotropy of the individual domains, we use $n = 2$, in accordance with its single-ion origin [53,54] and experimental data for Fe-Co-based amorphous alloys [55,56]. Then the laser-induced change of the magnetoelastic parameter is related to the demagnetization degree by

$$\frac{\Delta B_1(\Delta t)}{B_1} \approx 3\frac{\Delta M_S(\Delta t)}{M_S} + 3\left(\frac{\Delta M_S(\Delta t)}{M_S}\right)^2. \quad (3)$$

The ratio $\Delta B_1/B_1$ a few picoseconds after excitation is estimated to be -27% for $\Delta M_S/M_S = -10\%$. We note that the change of the magnetoelastic parameter is a nearly linear function of the degree of demagnetization when the latter is within 0%–15%.

Estimation of the laser-induced strain change is done based on the laser-induced increase in the ionic temperature $\Delta T \approx 300$ K (see Appendix B for details of the temperature estimation). The strains in the a_1 (a_2) domains change by $\Delta u_{xx}/u_{xx} \approx 124\%$ (-46%) and $\Delta u_{yy}/u_{yy} \approx -46\%$ (124%).

Figures 3 and 4 summarize the results of the calculations for the a_1 and a_2 domains when the external magnetic field is applied at $\varphi = -1^\circ$ and $\varphi = -45^\circ$ to the x axis. A misalignment $\varphi = -1^\circ$ is introduced to achieve better agreement between the measured and calculated field dependences of the precession frequency, and this is within the precision of the field alignment in the experiments. An equilibrium room temperature magnetization $M_S = 0.9 \times 10^6$ A/m and magnetoelastic parameter $B_1 = -22.8 \times 10^5$ mJ/cm^3 are used to obtain good agreement between the calculated and experimental field dependences of the precession frequency [Figs. 3(a) and 3(b)]. The magnetoelastic anisotropy energy associated with a 90° in-plane magnetization rotation $B_1(u_{yy} - u_{xx}) = -2.445 \times 10^4$ mJ/cm^3 and the magnetostriction coefficient $\lambda = 14.5 \times 10^{-6}$ agree with previous studies considering similar systems [25,57].

Figures 4(a), 4(c), and 4(d) show the calculated field dependence of the change of the equilibrium angle ψ_{eff} between $\mathbf{H}_{\text{eff}}$ and the x axis under laser excitation. Four scenarios are modeled, taking into account the ultrafast demagnetization ΔM_S only (orange dashed line), the decrease in the magnetoelastic parameter ΔB_1 only (green dashed line), the change in the strains Δu_{xx} and Δu_{yy} only (not shown), and the combination of all three (solid black line). As expected, ΔM_S and ΔB_1 result in opposite signs of $\Delta\psi_{\text{eff}}$. The effect of Δu_{xx} and Δu_{yy} appears to be more than 20 times smaller than that of ΔM_S and ΔB_1, in agreement with previous studies [58]. Indeed, the thermal expansion reduces the tensile in-plane strain and increases the compressive strain, thus affecting the magnetoelastic energy weakly. If all effects are combined, the laser-induced decrease in the magnetoelastic parameter

ΔB_1 dominates the magnetization response. The reorientation of the total effective field is therefore dictated by a *decrease* in the in-plane magnetoelastic anisotropy field H_{ME}.

In our model, the precession of the magnetization is excited, i.e., $\Delta\psi_{\mathrm{eff}} \neq 0$, over the whole field range studied in both domains at $\varphi = -45^\circ$ and only at low fields in the a_1 domain at $\varphi = -1^\circ$ [Figs. 4(a) and 4(c)]. The maximum absolute value of $\Delta\psi_{\mathrm{eff}}$ is close to 20° if $\varphi = -1^\circ$, while it is several times smaller at $\varphi = -45^\circ$. Taking into account the strong ellipticity ς of the excited precession, which depends on the strength and orientation of the applied field, we obtain the field dependences of the precession amplitudes $\Delta M_z^0/M_S$ shown in Figs. 3(c) and 3(d) by solid lines.

In Figs. 3(c) and 3(d), one sees that our model captures the general trend of the experimental field dependence of the precession amplitude. At $\varphi = -45^\circ$, there is reasonable agreement between the experiment and the model. At $\varphi = -1^\circ$, both the experiment and the model show a pronounced maximum of the precession amplitude at a low field and the absence of detectable precession at higher fields. However, at $\varphi = -1^\circ$ there are two discrepancies between the experimental and calculated amplitudes. The first one is *quantitative*, since the calculated amplitudes are larger than those obtained experimentally. Partly, this is related to the uncertainty in the static polar Kerr rotation (see Sec. II and Appendix A). This discrepancy can also be compensated by using a value of n smaller than 2 in the thermodynamic relation between magnetoelastic anisotropy and magnetization, which is often the case for real uniaxial materials.

More important is the *qualitative* difference between the experimental and calculated curves in Fig. 3(c). In our experiment, the precession amplitude is maximum at 30 mT, and no precession can be detected above a critical value of 50 mT. The model, in contrast, predicts that the maximum precession amplitude should be observed near the critical field, approximately 50 mT. Such behavior of the excited precession amplitude has indeed been seen in previous experiments on laser-induced precession in a hard-axis configuration [58]. Note that varying the parameter $n(n+1)/2$ in the model does not change the characteristic field at which the maximum amplitude is observed. Indeed, the excitation mechanism considered is nonresonant, and the maximum amplitude of the excited precession is achieved near a critical field where the magnetic system is most susceptible to any perturbation. Achieving the maximum precession amplitude at a different field and, correspondingly, at a different frequency would require, for instance, resonant driving of the magnetic system at that frequency [59]. Neither the thicknesses of the Au and $Co_{40}Fe_{40}B_{20}$ layers nor the periodicity of the domain pattern matches this scenario. Below, we argue that this qualitative difference is, in fact, an indication of laser-induced magnetization switching.

C. Magnetization dynamics triggered by change of magnetoelastic anisotropy

Excitation of magnetization precession by laser pulses is one of the possible pathways to achieving magnetization switching [60–62]. In particular, it has been shown that an ultrafast laser-driven decrease in magnetic anisotropy accompanied by a large-amplitude highly damped precession enables magnetization switching in an applied magnetic field [62]. If the deviation $\Delta\psi_{\mathrm{eff}}$ of the effective field from its equilibrium direction towards the applied magnetic field is large enough, and the in-plane magnetization component passes through the direction of the applied field after half of the period, switching is initiated. For such switching to be complete, the damping of the precession should be anomalously large to prevent the magnetization from returning to its initial orientation via further precessional motion [62]. Also, the restoration of the anisotropy should proceed on a time scale comparable to the precession frequency. Once such switching occurs, the stroboscopic pump-probe technique fails to correctly measure the amplitude of the excited precession, since this technique requires the sample to be in the very same initial state before excitation for each pump pulse.

The abrupt drop of the pump-probe signal detected at $\varphi = -1^\circ$ when the applied field reaches the critical value [Fig. 3(c)] may indicate that the amplitude of the excited precession is sufficiently large for precessional magnetization switching to be initiated. In Fig. 4, we illustrate this by plotting the maximum in-plane deviation of the magnetization from the x axis when (b) $\varphi = -1^\circ$ and (e) $\varphi = -45^\circ$. This deviation is calculated as $\psi_{\mathrm{eff}} - 2\Delta\psi_{\mathrm{eff}}$ [see the insets in Figs. 4(b) and 4(e)]. Above $H_{\mathrm{ext}} \approx 40$ mT, the first condition for magnetization switching is satisfied for $\varphi = -1^\circ$ [see the gray area in Fig. 3(c)]. At $\varphi = -45^\circ$, this deviation is large at any external magnetic field, and no switching is expected.

In order to analyze whether such a reorientation of the effective field can result in switching of the magnetization, we simulate the trajectory of the magnetization motion in response to the abrupt decrease and subsequent restoration of M_S and B_1. The simulations are performed by solving the LLG equation for a macrospin. The external field is applied along the hard magnetization axis (x axis). The time-dependent effective field entering the LLG equation is calculated using Eq. (2) and taking into account the relaxation of the laser-induced demagnetization found in our experiments [see Figs. 2(b) and 5(a)]. The temporal evolution of ΔB_1 is found accordingly using Eq. (3). Also, slower relaxation of M_S and B_1 towards equilibrium is considered, as shown in Fig. 5(b). The Gilbert damping

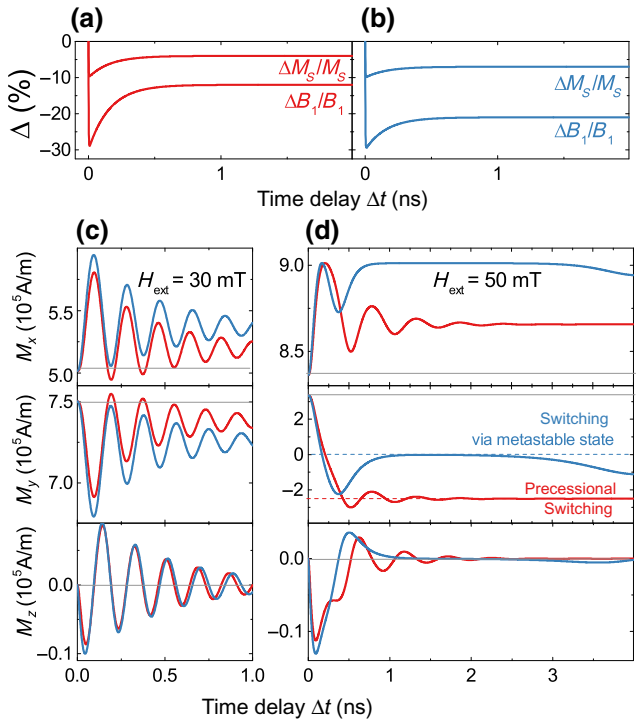

FIG. 5. Modeling of laser-induced magnetization precession when the magnetic field $\mathbf{H}_{ext}$ is applied along the hard (x) axis. (a),(b) Evolution of the magnetization M_S and magnetoelastic parameter B_1 used in the modeling, (a) with relaxation similar to that observed in the experiment [Fig. 2(b)] and (b) with a slower relaxation. (c),(d) Dynamics of components $M_{x,y,z}$ of the magnetization at (c) $H_{ext} = 30$ mT and (d) $H_{ext} = 50$ mT. The results are obtained by using the faster (red lines) and slower (blue lines) evolutions of M_S and B_1 shown in (a),(b), respectively. The solid gray lines indicate the equilibrium orientation of the magnetization. The red and blue dashed lines indicate the switched state and metastable state ($\mathbf{M}\|\mathbf{H}_{ext}$), respectively.

parameter $\alpha = 0.02$ is chosen to match the precession decay observed far from the critical field.

In Fig. 5, we show the simulated magnetization trajectories represented by the evolution of the x,y,z components of the magnetization at $H_{ext} = 30$ and 50 mT. As one can see in Fig. 5(c), at $H_{ext} = 30$ mT the laser excitation results in a decaying magnetization precession. Changing the details of the relaxation of M_S and B_1 towards equilibrium has only a small effect on the excited dynamics [compare the red and blue curves in Fig. 5(c)]. At $H_{ext} = 50$ mT [Fig. 5(d)], the amplitude of the excited precession is large enough, and the condition for the initiation of precessional switching is fulfilled. The subsequent dynamics is strongly dependent on the relaxation of the total effective field towards its equilibrium value, and we get either precessional switching [red lines in Fig. 5(d)] or temporal trapping of the magnetization in metastable local state. The subsequent cooling down of the system results in either a return of the magnetization to its initial orientation or magnetic switching to another stable direction [blue lines in Fig. 5(d)]. This leads to a situation where only some of the excitation events result in switching.

Importantly, once the magnetization has switched from one equilibrium orientation to another, the next pump pulse will again excite precession and switching. However, the M_z component will oscillate with a shift in phase of π compared with the oscillations excited by the preceding pump pulse. Our pump-probe experiments are stroboscopic and average the dynamics of M_z, which is repetitively driven by approximately 10^4 pump pulses. Therefore, the switching described above is seen as a reduction of the detected signal amplitude. At 50% switching events, no oscillatory signal will be detected. Furthermore, the Gaussian spatial profile of the pump pulse causes switching in the center of the spot at a lower average fluence compared with the outer part. This, in particular, should result in concentric ringlike structures with switched and nonswitched areas, which are a characteristic feature of precessional switching driven by spatially inhomogeneous stimuli [62–64]. Detection of such switching requires single-shot pump-probe imaging [34], for which the strength of the magneto-optical signal in a $Co_{40}Fe_{40}B_{20}/BaTiO_3$ structure is insufficient. Nevertheless, we argue that the noticeable decrease in the detected amplitude of the precession at applied fields exceeding 30 mT seen in our experiments is a manifestation of precessional switching of magnetization triggered by an ultrafast decrease in the magnetoelastic parameter.

V. CONCLUSIONS

In conclusion, we show that the magnetoelastic coupling in a metallic $Co_{40}Fe_{40}B_{20}$ film can be significantly reduced on a picosecond time scale by excitation with a femtosecond laser pulse. This effect is explained by a simple model, which accounts for a laser-induced increase in the electronic and ionic temperatures and relates the induced changes of the magnetoelastic parameter and magnetization via an $n(n+1)/2$ law. This law appears to hold for laser-induced processes in metals on time scales beyond several picoseconds following excitation; such a time scale is required for establishing a quasiequilibrium between the electronic, ionic, and spin subsystems. The demonstrated ability to decrease the magnetoelastic parameter with laser pulses enables the driving of magnetization dynamics in metallic films in which the magnetoelastic anisotropy dominates. We employ this mechanism to experimentally realize selective excitation of magnetization precession in individual micrometer-size magnetic stripe domains imprinted in a $Co_{40}Fe_{40}B_{20}$ film by a ferroelectric $BaTiO_3$ substrate. We find that the excitation of precession in an individual $Co_{40}Fe_{40}B_{20}$ domain is controlled by the strength and the orientation of the applied magnetic field with respect to the

local uniaxial-anisotropy axis. This allows us, in particular, to distinguish magnetization precessions in separate domains even when they are unresolvable in static measurements due to a large applied magnetic field. Further, we show that a change of the magnetoelastic anisotropy can even trigger precessional switching of the magnetization in a selected domain, which is manifested in the pump-probe experiments as a suppression of the detected precession. Precessional switching is realized near a critical field of 50 mT applied along the hard magnetization axis of the domain.

Our results therefore show that structures consisting of $Co_{40}Fe_{40}B_{20}$ on a ferroelectric or piezoelectric substrate are prospective candidates for optically driven precessional switching via anomalously damped precession [62] under application-relevant conditions. Indeed, the specific anisotropy and damping required for the switching may be tailored in such heterostructures both during the growth stage and afterwards. Namely, a ferroelectric or piezoelectric substrate enables one to control the orientation and strength of the magnetic anisotropy with an external voltage, while the damping in the $Co_{40}Fe_{40}B_{20}$ may be tuned by various means, such as annealing and variation of the composition [65,66].

The possibility of altering the magnetoelastic parameter with laser pulses can be exploited further both in FM-FE composites and in heterostructures formed from FM and piezoelectric constituents. A decrease in B_1 reduces the strain-mediated magnetoelectric coupling in multiferroic and magnetoelectric heterostructures, which could enable laser-assisted magnetization switching with an applied electric field with submicrometer spatial resolution [17], in analogy to heat-assisted magnetic recording. Moreover, in strained films a spin-reorientation transition can occur due to an extra contribution to the out-of-plane anisotropy [Eq. (1)] controlled by the magnetoelastic parameter [40]. Hence, laser excitation may be used to trigger such a transition on a picosecond time scale via changes of B_1 and the film strain. Finally, laser-induced changes of magnetoelastic anisotropy may be employed for driving spin waves [67] in switchable magnonic waveguides based on $Co_{40}Fe_{40}B_{20}/BaTiO_3$ structures [25,27,68,69].

ACKNOWLEDGMENTS

We thank N. E. Khokhlov and P. I. Gerevenkov for fruitful discussions. The TEM study was carried out using a Jeol JEM-2100F microscope at the Federal Joint Research Center "Materials Science and Characterization in Advanced Technologies." L.A.Sh., A.V.Sch., and A.M.K. acknowledge the RSF (Grant No. 16-12-10485) for support for the experimental studies, and the RFBR (Grant No. 19-52-12065) and the DFG program TRR160 ICRC for support for the theoretical work. LLG-based modeling was performed by L.A.Sh. and A.M.K. under support of the RSF (Grant No. 20-12-00309). S.J.H. and S.v.D. were supported by the Academy of Finland (Grant No. 316857). The collaboration between the Ioffe Institute and Aalto University is a part of the COST Action CA17123 Magnetofon.

APPENDIX A: STATIC POLAR AND LONGITUDINAL MOKE IN $Co_{40}Fe_{40}B_{20}/BaTiO_3$

In the experiment, we measure the static longitudinal Kerr rotation θ_S^L and the ellipticity ϵ_S^L with an in-plane-saturated sample. Using the general formulas for the longitudinal Kerr effect [70], we find the magneto-optical parameter Q from

$$Q = (i\theta_S^L + \epsilon_S^L)/A_L, \tag{A1}$$

where

$$A_L = \frac{\eta^2 \sin\zeta(\sin\zeta\tan\zeta - \sqrt{\eta^2 - \sin^2\zeta})}{(\eta^2-1)(\eta^2-\tan^2\zeta)\sqrt{\eta^2-\sin^2\zeta}}.$$

Here, $\zeta = 45^\circ$ is the angle of incidence used in the longitudinal MOKE experiment; $\eta = n_2/n_1$, where n_1 and n_2 are refractive indices of gold and $Co_{40}Fe_{40}B_{20}$, respectively, at the probe wavelength of 1030 nm.

Knowing Q, one can calculate the polar Kerr rotation θ_S^P corresponding to the fully out-of-plane-saturated film as

$$\theta_S^P = \mathrm{Im}\{QA_P\}, \tag{A2}$$

where

$$A_P = \frac{\eta^2(\sin\zeta\tan\zeta + \sqrt{\eta^2 - \sin^2\zeta})}{(\eta^2-1)(\eta^2-\tan^2\zeta)}.$$

Here, $\zeta = 17^\circ$ is the angle of incidence used in the main experiments. The coefficients A_L and A_P are written for the p polarization.

We are not aware of any data on the refractive index of $Co_{40}Fe_{40}B_{20}$ at 1030 nm. In Ref. [71], a refractive index $n_2 = 4 + i4.7$ for $Co_{20}Fe_{60}B_{20}$ films at 1030 nm was reported. Comparison of the spectra of the complex refractive indices of as-deposited $Co_{20}Fe_{60}B_{20}$ [71] and $Co_{60}Fe_{20}B_{20}$ [72] for wavelengths of 400–800 nm suggests that the optical properties of the alloy do not vary strongly within this composition range. However, the optical properties of $Co_{40}Fe_{40}B_{20}$ films depend on the crystallinity of the film [72]. Furthermore, the optical parameters of thin gold layers are dependent on the substrate, thickness, etc. [73].

Using the values $n_2 = 4 + i4.7$ for $Co_{40}Fe_{40}B_{20}$ and $n_1 = 1.5 + i5.3$ reported for an 11-nm-thick gold film [73], we get an estimate for the polar Kerr rotation $\theta_S^P \approx 15$ mdeg. Taking different optical parameters of $Co_{40}Fe_{40}B_{20}$ and Au may increase or decrease the estimated θ_S^P.

APPENDIX B: LASER-INDUCED HEATING OF $Co_{40}Fe_{40}B_{20}$ LAYER

For the estimation of the ultrafast laser-induced heating of the $Co_{40}Fe_{40}B_{20}$ layer in the $Au/Co_{40}Fe_{40}B_{20}/BaTiO_3$ structure, we use the following parameters. The complex refractive index of the capping gold layer is $n_1 = 0.51 + i2.02$ at the pump wavelength of 515 nm [73]. This gives an intensity reflection coefficient $R_1 = 0.68$ at the air/Au interface. The absorption coefficient of the gold film is $\alpha_1 = 4.28 \times 10^5\ \mathrm{cm}^{-1}$. The complex refractive index of the $Co_{40}Fe_{40}B_{20}$ is $n_2 = 2.5 + i3.25$ at 515 nm [71,72], which gives an intensity reflection coefficient at the $Au/Co_{40}Fe_{40}B_{20}$ interface $R_2 = 0.148$. The absorption coefficient of the $Co_{40}Fe_{40}B_{20}$ is $\alpha_2 = 7.93 \times 10^5\ \mathrm{cm}^{-1}$.

The temperature increase in the $Co_{40}Fe_{40}B_{20}$ layer is found from

$$\Delta T = (1 - R_1)e^{-\alpha_1 d}(1 - R_2)\alpha_2(1 - e^{-1})\frac{J}{C\rho}, \qquad \text{(B1)}$$

where $C = 440\ \mathrm{J\,kg^{-1}\,K^{-1}}$ is the heat capacity [74] and $\rho = 7.7 \times 10^3\ \mathrm{kg\,m^{-3}}$ is the density of $Co_{40}Fe_{40}B_{20}$ [75], and d is the thickness of the Au layer. The factor $\alpha_2(1 - e^{-1})J$ gives the volume energy density in the case where the film thickness exceeds the light penetration depth [76]. For an incident fluence $J = 10\ \mathrm{mJ/cm^2}$, one gets a laser-induced heating $\Delta T \approx 300\ \mathrm{K}$. Accounting for the additional scattering of light that takes place at the $Au/Co_{40}Fe_{40}B_{20}$ interface may reduce the amount of energy deposited in the $Co_{40}Fe_{40}B_{20}$ and the corresponding heating.

[1] G. A. Smolenskiĭ and I. E. Chupis, Ferroelectromagnets, Sov. Phys.: Uspekhi **25**, 475 (1982).

[2] M. Fiebig, Revival of the magnetoelectric effect, J. Phys. D: Appl. Phys. **38**, R123 (2005).

[3] J.-M. Hu, L.-Q. Chen, and C.-W. Nan, Multiferroic heterostructures integrating ferroelectric and magnetic materials, Adv. Mater. **28**, 15 (2015).

[4] S. Manipatruni, D. E. Nikonov, C.-C. Lin, T. A. Gosavi, H. Liu, B. Prasad, Y.-L. Huang, E. Bonturim, R. Ramesh, and I. A. Young, Scalable energy-efficient magnetoelectric spin–orbit logic, Nature **565**, 35 (2019).

[5] Z. Chu, M. PourhosseiniAsl, and S. Dong, Review of multi-layered magnetoelectric composite materials and devices applications, J. Phys. D: Appl. Phys. **51**, 243001 (2018).

[6] N. A. Hill, Why are there so few magnetic ferroelectrics? J. Phys. Chem. B **104**, 6694 (2000).

[7] C. A. F. Vaz, Electric field control of magnetism in multiferroic heterostructures, J. Phys. Condens. Matter **24**, 333201 (2012).

[8] Y. Wang, J. Hu, Y. Lin, and C.-W. Nan, Multiferroic magnetoelectric composite nanostructures, NPG Asia Mater. **2**, 61 (2010).

[9] G. P. Carman and N. Sun, Strain-mediated magnetoelectrics: Turning science fiction into reality, MRS Bull. **43**, 822 (2018).

[10] C.-W. Nan, M. I. Bichurin, S. Dong, D. Viehland, and G. Srinivasan, Multiferroic magnetoelectric composites: Historical perspective, status, and future directions, J. Appl. Phys. **103**, 031101 (2008).

[11] T. Taniyama, K. Akasaka, D. Fu, M. Itoh, H. Takashima, and B. Prijamboedi, Electrical voltage manipulation of ferromagnetic microdomain structures in a ferromagnetic/ferroelectric hybrid structure, J. Appl. Phys. **101**, 09F512 (2007).

[12] T. H. E. Lahtinen, J. O. Tuomi, and S. van Dijken, Pattern transfer and electric-field-induced magnetic domain formation in multiferroic heterostructures, Adv. Mater. **23**, 3187 (2013).

[13] Y. Shirahata, R. Shiina, D. L. González, K. J. A. Franke, E. Wada, M. Itoh, N. A. Pertsev, S. van Dijken, and T. Taniyama, Electric-field switching of perpendicularly magnetized multilayers, NPG Asia Mater. **7**, e198 (2015).

[14] T. H. E. Lahtinen, K. J. A. Franke, and S. Van Dijken, Electric-field control of magnetic domain wall motion and local magnetization reversal, Sci. Rep. **2**, 258 (2012).

[15] M. Buzzi, R. V. Chopdekar, J. L. Hockel, A. Bur, T. Wu, N. Pilet, P. Warnicke, G. P. Carman, L. J. Heyderman, and F. Nolting, Single Domain Spin Manipulation by Electric Fields in Strain Coupled Artificial Multiferroic Nanostructures, Phys. Rev. Lett. **111**, 027204 (2013).

[16] K. J. A. Franke, B. Van de Wiele, Y. Shirahata, S. J. Hämäläinen, T. Taniyama, and S. van Dijken, Reversible Electric-Field-Driven Magnetic Domain-Wall Motion, Phys. Rev. X **5**, 011010 (2015).

[17] R. LoConte, J. Gorchon, A. Mougin, C. H. A. Lambert, A. El-Ghazaly, A. Scholl, S. Salahuddin, and J. Bokor, Electrically controlled switching of the magnetization state in multiferroic $BaTiO_3$/CoFe submicrometer structures, Phys. Rev. Mater. **2**, 091402 (R) (2018).

[18] C. Cavaco, M. Van Kampen, L. Lagae, and G. Borghs, A room-temperature electrical field–controlled magnetic memory cell, J. Mater. Res. **22**, 2111 (2007).

[19] N. A. Pertsev and H. Kohlstedt, Magnetic tunnel junction on a ferroelectric substrate, Appl. Phys. Lett. **95**, 163503 (2009).

[20] N. A. Pertsev and H. Kohlstedt, Resistive switching via the converse magnetoelectric effect in ferromagnetic multilayers on ferroelectric substrates, Nanotechnology **21**, 475202 (2010).

[21] M. Liu, S. Li, O. Obi, J. Lou, S. Rand, and N. X. Sun, Electric field modulation of magnetoresistance in multiferroic heterostructures for ultralow power electronics, Appl. Phys. Lett. **98**, 222509 (2011).

[22] A. Chen, Y. Wen, B. Fang, Y. Zhao, Q. Zhang, Y. Chang, P. Li, H. Wu, H. Huang, Y. Lu, Z. Zeng, J. Cai, X. Han, T. Wu, X.-X. Zhang, and Y. Zhao, Giant nonvolatile manipulation of magnetoresistance in magnetic tunnel junctions by electric fields via magnetoelectric coupling, Nat. Commun. **10**, 243 (2019).

[23] M. Liu, Z. Zhou, T. Nan, B. M. Howe, G. J. Brown, and N. X. Sun, Voltage tuning of ferromagnetic resonance

with bistable magnetization switching in energy-efficient magnetoelectric composites, Adv. Mater. **25**, 1435 (2013).

[24] J. Lou, M. Liu, D. Reed, Y. Ren, and N. X. Sun, Giant electric field tuning of magnetism in novel multiferroic FeGaB/lead zinc niobate–lead titanate (PZN-PT) heterostructures, Adv. Mater. **21**, 4711 (2009).

[25] F. Brandl, K. J. A. Franke, T. H. E. Lahtinen, S. van Dijken, and D. Grundler, Spin waves in CoFeB on ferroelectric domains combining spin mechanics and magnonics, Solid State Commun. **198**, 13 (2014).

[26] A. V. Azovtsev and N. A. Pertsev, Electrical Tuning of Ferromagnetic Resonance in Thin-Film Nanomagnets Coupled to Piezoelectrically Active Substrates, Phys. Rev. Appl. **10**, 044041 (2018).

[27] S. J Hämäläinen, M. Madami, H. Qin, G. Gubbiotti, and S. van Dijken, Control of spin-wave transmission by a programmable domain wall, Nat. Commun. **9**, 4853 (2018).

[28] A. V. Sadovnikov, A. A. Grachev, S. E. Sheshukova, Yu. P. Sharaevskii, A. A. Serdobintsev, D. M. Mitin, and S. A. Nikitov, Magnon Straintronics: Reconfigurable Spin-Wave Routing in Strain-Controlled Bilateral Magnetic Stripes, Phys. Rev. Lett. **120**, 257203 (2018).

[29] E. O. Savostin and N. A. Pertsev, Superconducting straintronics via the proximity effect in superconductor–ferromagnet nanostructures, Nanoscale **12**, 648 (2020).

[30] A. Kirilyuk, A. V. Kimel, and Th. Rasing, Ultrafast optical manipulation of magnetic order, Rev. Mod. Phys. **82**, 2731 (2010).

[31] Y. M. Sheu, S. A. Trugman, L. Yan, Q. X. Jia, A. J. Taylor, and R. P. Prasankumar, Using ultrashort optical pulses to couple ferroelectric and ferromagnetic order in an oxide heterostructure, Nat. Commun. **5**, 5832 (2014).

[32] C. Jia, N. Zhang, A. Sukhov, and J. Berakdar, Ultrafast transient dynamics in composite multiferroics, New J. Phys. **18**, 023002 (2016).

[33] M. Lejman, G. Vaudel, I. C. Infante, P. Gemeiner, V. E. Gusev, B. Dkhil, and P. Ruello, Giant ultrafast photo-induced shear strain in ferroelectric $BiFeO_3$, Nat. Commun. **5**, 4301 (2014).

[34] A. V. Kimel, A. M. Kalashnikova, A. Pogrebna, and A. K. Zvezdin, Fundamentals and perspectives of ultrafast photoferroic recording, Phys. Rep. **852**, 1 (2020).

[35] H.-J. Liu, L.-Y. Chen, Q. He, C.-W. Liang, Y.-Z. Chen, Y.-S. Chien, Y.-H. Hsieh, S.-J. Lin, E. Arenholz, C.-W. Luo, Y.-L. Chueh, Y.-C. Chen, and Y.-H. Chu, Epitaxial photostriction–magnetostriction coupled self-assembled nanostructures, ACS Nano **6**, 6952 (2012).

[36] J.-Y. Bigot, M. Vomir, L. H. F. Andrade, and E. Beaurepaire, Ultrafast magnetization dynamics in ferromagnetic cobalt: The role of the anisotropy, Chem. Phys. **318**, 137 (2005).

[37] E. Carpene, E. Mancini, D. Dazzi, C. Dallera, E. Puppin, and S. De Silvestri, Ultrafast three-dimensional magnetization precession and magnetic anisotropy of a photoexcited thin film of iron, Phys. Rev. B **81**, 060415(R) (2010).

[38] E. Carpene, E. Mancini, C. Dallera, E. Puppin, and S. De Silvestri, Three-dimensional magnetization evolution and the role of anisotropies in thin Fe/MgO films: Static and dynamic measurements, J. Appl. Phys. **108**, 063919 (2010).

[39] L. A. Shelukhin, V. V. Pavlov, P. A. Usachev, P. Yu. Shamray, R. V. Pisarev, and A. M. Kalashnikova, Ultrafast laser-induced changes of the magnetic anisotropy in a low-symmetry iron garnet film, Phys. Rev. B **97**, 014422 (2018).

[40] N. A. Pertsev, Giant magnetoelectric effect via strain-induced spin reorientation transitions in ferromagnetic films, Phys. Rev. B **78**, 212102 (2008).

[41] J. P. Hirth and J. Lothe, *Theory of Dislocations* (McGraw-Hill, New York, 1968).

[42] Y. S. Touloukian, R. W. Powell, C. Y. Ho, and P. G. Klemens, *Thermophysical Properties of Matter-The TPRC Data Series. Volume 2. Thermal Conductivity-Nonmetallic Solids* (IFI/Plenum, New York, 1970).

[43] K. An, X. Ma, C.-F. Pai, J. Yang, K. S. Olsson, J. L. Erskine, D. C. Ralph, R. A. Buhrman, and X. Li, Current control of magnetic anisotropy via stress in a ferromagnetic metal waveguide, Phys. Rev. B **93**, 140404(R) (2016).

[44] O. Madelung, U. Rössler, and M. Schulz, in *Ternary Compounds, Organic Semiconductors* (Springer-Verlag, Berlin, Heidelberg, 2000).

[45] H. F. Kay and P. Vousden, XCV. Symmetry changes in barium titanate at low temperatures and their relation to its ferroelectric properties, Philos. Mag. **40**, 1019 (1949).

[46] E. Beaurepaire, J.-C. Merle, A. Daunois, and J.-Y. Bigot, Ultrafast Spin Dynamics in Ferromagnetic Nickel, Phys. Rev. Lett. **76**, 4250 (1996).

[47] B. Koopmans, G. Malinowski, F. Dalla Longa, D. Steiauf, M. Fähnle, T. Roth, M. Cinchetti, and M. Aeschlimann, Explaining the paradoxical diversity of ultrafast laser-induced demagnetization, Nat. Mater. **9**, 259 (2010).

[48] M. van Kampen, C. Jozsa, J. T. Kohlhepp, P. LeClair, L. Lagae, W. J. M. de Jonge, and B. Koopmans, All-Optical Probe of Coherent Spin Waves, Phys. Rev. Lett. **88**, 227201 (2002).

[49] A. G. Gurevich and G. A. Melkov, *Magnetization Oscillations and Waves* (CRC Press, Boca Raton, 1996).

[50] J. Smit and H. G. Beljers, Ferromagnetic resonance absorption in $BaFe_{12}O_{19}$, a highly anisotropic crystal, Philips Res. Repts **10**, 113 (1955).

[51] H. Suhl, Ferromagnetic resonance in nickel ferrite between one and two kilomegacycles, Phys. Rev. **97**, 555 (1955).

[52] E. R. Callen and H. B. Callen, Anisotropic magnetization, J. Phys. Chem. Solids **16**, 310 (1960).

[53] C. Kittel and J. H. Van Vleck, Theory of the temperature dependence of the magnetoelastic constants of cubic crystals, Phys. Rev. **118**, 1231 (1960).

[54] E. Callen and H. B. Callen, Magnetostriction, forced magnetostriction, and anomalous thermal expansion in ferromagnets, Phys. Rev. **139**, A455 (1965).

[55] R. C. O'Handley, Temperature dependence of magnetostriction in $Fe_{80}B_{20}$ glass, Solid State Commun. **22**, 485 (1977).

[56] J. M. Barandiarán, J. Gutiérrez, and A. García-Arribas, Magneto-elasticity in amorphous ferromagnets: Basic principles and applications, Phys. Status Solidi (A) **208**, 2258 (2011).

[57] S. Isogami and T. Taniyama, Strain mediated in-plane uniaxial magnetic anisotropy in amorphous CoFeB films based on structural phase transitions of $BaTiO_3$ single-crystal substrates, Phys. Status Solidi (A) **215**, 1700762 (2018).

[58] V. N. Kats, T. L. Linnik, A. S. Salasyuk, A. W. Rushforth, M. Wang, P. Wadley, A. V. Akimov, S. A. Cavill, V. Holy, A. M. Kalashnikova, and A. V. Scherbakov, Ultrafast changes of magnetic anisotropy driven by laser-generated coherent and noncoherent phonons in metallic films, Phys. Rev. B **93**, 214422 (2016).

[59] J. V. Jäger, A. V. Scherbakov, B. A. Glavin, A. S. Salasyuk, R. P. Campion, A. W. Rushforth, D. R. Yakovlev, A. V. Akimov, and M. Bayer, Resonant driving of magnetization precession in a ferromagnetic layer by coherent monochromatic phonons, Phys. Rev. B **92**, 020404(R) (2015).

[60] E. Carpene, C. Piovera, C. Dallera, E. Mancini, and E. Puppin, All-optical subnanosecond coherent spin switching in thin ferromagnetic layers, Phys. Rev. B **84**, 134425 (2011).

[61] A. Stupakiewicz, K. Szerenos, D. Afanasiev, A. Kirilyuk, and A. V. Kimel, Ultrafast nonthermal photo-magnetic recording in a transparent medium, Nature **542**, 71 (2017).

[62] C. S. Davies, K. H. Prabhakara, M. D. Davydova, K. A. Zvezdin, T. B. Shapaeva, S. Wang, A. K. Zvezdin, A. Kirilyuk, Th. Rasing, and A. V. Kimel, Anomalously Damped Heat-Assisted Route for Precessional Magnetization Reversal in an Iron Garnet, Phys. Rev. Lett. **122**, 027202 (2019).

[63] I. Tudosa, C. Stamm, A. B. Kashuba, F. King, H. C. Siegmann, J. Stöhr, G. Ju, B. Lu, and D. Weller, The ultimate speed of magnetic switching in granular recording media, Nature **428**, 831 (2004).

[64] J. A. de Jong, I. Razdolski, A. M. Kalashnikova, R. V. Pisarev, A. M. Balbashov, A. Kirilyuk, Th. Rasing, and A. V. Kimel, Coherent Control of the Route of an Ultrafast Magnetic Phase Transition via Low-Amplitude Spin Precession, Phys. Rev. Lett. **108**, 157601 (2012).

[65] Y. Zhang, X. Fan, W. Wang, X. Kou, R. Cao, X. Chen, Ch. Ni, L. Pan, and J. Q. Xiao, Study and tailoring spin dynamic properties of CoFeB during rapid thermal annealing, Appl. Phys. Lett. **98**, 042506 (2011).

[66] S. Srivastava, A. P. Chen, T. Dutta, R. Ramaswamy, J. Son, M. S. M. Saifullah, K. Yamane, K. Lee, K.-L. Teo, Y. P. Feng, and H. Yang, Effect of $(Co_xFe_{1-x})_{80}B_{20}$ Composition on the Magnetic Properties of the Free Layer in Double-Barrier Magnetic Tunnel Junctions, Phys. Rev. Appl. **10**, 024031 (2018).

[67] N. E. Khokhlov, P. I. Gerevenkov, L. A. Shelukhin, A. V. Azovtsev, N. A. Pertsev, M. Wang, A. W. Rushforth, A. V. Scherbakov, and A. M. Kalashnikova, Optical Excitation of Propagating Magnetostatic Waves in an Epitaxial Galfenol Film by Ultrafast Magnetic Anisotropy Change, Phys. Rev. Appl. **12**, 044044 (2019).

[68] B. Van de Wiele, S. J. Hämäläinen, P. Baláž, F. Montoncello, and S. Van Dijken, Tunable short-wavelength spin wave excitation from pinned magnetic domain walls, Sci. Rep. **6**, 21330 (2016).

[69] D. López González, A. Casiraghi, B. Van de Wiele, and S. Van Dijken, Reconfigurable magnetic logic based on the energetics of pinned domain walls, Appl. Phys. Lett. **108**, 032402 (2016).

[70] A. K. Zvezdin and V. K. Kotov, *Modern Magnetooptics and Magnetooptical Materials* (IoP Publishing, Bristol, Philadelphia, 1997).

[71] X. Liang, X. Xu, R. Zheng, Z. A. Lum, and J. Qiu, Optical constant of CoFeB thin film measured with the interference enhancement method, Appl. Opt. **54**, 1557 (2015).

[72] M. A. Hoffmann, A. Sharma, P. Matthes, S. Okano, O. Hellwig, R Ecke, D. R. T. Zahn, G. Salvan, and S. E. Schulz, Spectroscopic ellipsometry and magneto-optical Kerr effect spectroscopy study of thermally treated $Co_{60}Fe_{20}B_{20}$ thin films, J. Phys. Condens. Matter **32**, 055702 (2019).

[73] G. Rosenblatt, B. Simkhovich, G. Bartal, and M. Orenstein, Nonmodal Plasmonics: Controlling the Forced Optical Response of Nanostructures, Phys. Rev. X **10**, 011071 (2020).

[74] M. Walter, J. Walowski, V. Zbarsky, M. Münzenberg, M. Schäfers, D. Ebke, G. Reiss, A. Thomas, P. Peretzki, M. Seibt, J. S. Moodera, M. Czerner, M. Bachmann, and C. Heiliger, Seebeck effect in magnetic tunnel junctions, Nat. Mater. **10**, 742 (2011).

[75] R. C. O'Handley, R. Hasegawa, R. Ray, and C.-P. Chou, Ferromagnetic properties of some new metallic glasses, Appl. Phys. Lett. **29**, 330 (1976).

[76] J. Walowski, Ph.D. thesis, School Niedersächsische Staats- und Universitätsbibliothek Göttingen, 2012.